Supporting Information

Title: Kinetics of Zero Valent Iron Nanoparticle Oxidation in Oxygenated Water

Authors:

Lauren F. Greenlee

Jessica D. Torrey

Robert L. Amaro

Justin M. Shaw

Applied Chemicals and Materials Division

Electromagnetics Division

National Institute of Standards and Technology

325 Broadway

Boulder, CO 80305

USA

The Supporting Information contains 35 pages, 9 figures and 1 table.

I. MATERIALS AND METHODS: DETAILS

A. Chemicals

The iron salt used was ferrous sulfate heptahydrate ($FeSO_4*7H_2O$), and the nickel salt used was nickel chloride hexahydrate ($NiCl_2*6H_2O$). Sodium borohydride ($NaBH_4$) was used as the reducing agent. Two organic stabilizers, carboxymethyl cellulose (CMC) and amino tri(methylene phosphonic acid) (ATMP), were used during nanoparticle synthesis to prevent particle agglomeration. The CMC compound used had a molecular weight of 250,000 g/mol and a carboxylate degree of substitution of 0.7. A stock solution of 10 g/L CMC was made by dissolving dry CMC in purified water heated to 60 ^oC to 70 ^oC. The ATMP (molecular weight = 298 g/mol) was in the form of the pentasodium salt in aqueous solution.

B. Nanoparticle Synthesis

ZVI nanoparticles were synthesized in argon-bubbled aqueous solution with ferrous sulfate as the iron source and sodium borohydride as the reducing agent. In a typical synthesis [1, 2], stabilizer and iron salt were added to purified water and bubbled for 15 min with argon in a three-neck round bottom flask. The solution was constantly mixed at 100 rpm with an orbital shaker. A molar ratio of 2.2:1 was used for sodium borohydride to iron, and the sodium borohydride was added to the iron salt solution dropwise with a syringe. The molar ratio of borohydride to iron was chosen based on the stoichiometric requirement for the reduction of ferrous iron to iron metal, and the 10 % excess of borohydride was added to account for the loss of some of the borohydride due to a competing reaction with water molecules. The reaction was allowed to proceed to completion under vacuum. For bimetallic ZVI-Ni nanoparticles, a solution of nickel chloride and stabilizer was added dropwise to the suspension to deposit a nickel shell on the ZVI nanoparticles. The suspension was allowed to react for an additional 15 min under

vacuum. Nickel deposition onto iron metal is auto-catalytic due to the difference in standard reduction potential, E^0, of the two metals ($E^0(Fe^{2+})$ = -0.44 V and $E^0(Ni^{2+})$ = -0.25 V). The nanoparticle suspension was then collected and centrifuged at 18,000 relative centrifugal force (rcf) for one hour to separate the particles from the aqueous supernatant. The particles were resuspended in methanol by sonication. The stabilizers were used at ratios of 0.05 mol:mol Fe and 0.0005 mol:mol Fe for ATMP and CMC, respectively. The bimetallic nanoparticles were synthesized at ratios from 0.5 mmol Ni:mol Fe to 1000 mmol Ni:mol Fe.

C. Nanoparticle Characterization

Field emission scanning electron microscopy (FESEM) samples were prepared by drop casting a dilution of the methanol nanoparticle suspension onto a silicon wafer. Energy dispersive x-ray spectroscopy (EDX) was performed on FESEM samples to determine the relative rations of iron, nickel, and oxygen in the iron-nickel nanoparticles. Powder X-ray diffraction (XRD) samples were prepared by centrifuging the methanol suspension, resuspending the nanoparticles in a small volume of methanol (approximately 30 μL), and drop casting onto a silicon substrate. Transmission electron microscopy (TEM) samples were cast onto an ultrathin carbon film on supported by lacey carbon on a copper grid, similar to the FESEM samples. All oxidized samples were prepared with the same methods after oxidation of the nanoparticles occurred. Bulk aqueous ZVI nanoparticle suspensions were shaken to oxidize the particles before XRD analysis.

D. Experiments for Kinetic Modeling

The DLS instrument used in this work correlated laser light (He-Ne, wavelength 633 nm, power 4 mW) scattered at 173^o with Mie theory to determine the particle size of the sample. The direct measurement of scattered light intensity was used to determine the change in particle

diameter (*i.e.,* hydrodynamic diameter) over time. The DLS measurement assumes a spherical particle for all measurements. To start the measurement, a 20 μL aliquot from the methanol nanoparticle suspension was added into a 10 mL volume of water and ethanol; volumetric ratios of 0, 25:75, and 50:50 ethanol:water were tested. The sample was pumped through the DLS sample cell at a rate of 800 μL/min, and flow was stopped periodically to take measurements of size and zeta potential. The QCM technique employed gold-plated quartz crystals with a resonance frequency of 5 MHz. The crystals were spray coated with nanoparticles from the methanol suspension with a gravity-fed airbrush operated at 207 kPa (30 psi). Initial sample mass ranged between 5 μg and 20 μg. Each crystal received two consecutive coats with the airbrush held at a distance of 15 mm. The coated crystals were then placed in flow cells within the QCM, and flow experiments were conducted at flow rates of 50 μL/min and 500 μL/min. ZVI nanoparticles were tested for volumetric ratios of 0, 25:75, 50:50, and 90:10 ethanol:water, while Fe-Ni nanoparticles were only tested in purified water (oxygenated throughout experiments using a stir bar and stir plate). The pH of the purified water was within the range of 6.5 to 7.0. All experiments were performed at room temperature.

The QCM technique measures the resonance frequency of the quartz crystal, and the change in frequency can be directly related to the change in mass of the sample through the Sauerbrey equation [3].

II. THEORETICAL BASIS FOR KINETIC MODELING

A. High-temperature Oxidation

High-temperature, diffusion-controlled metal oxidation in the presence of oxygen gas may be described by a parabolic rate law and is directly derived from Fick's laws of diffusion [4, 5].

Wagner [4] derived parabolic oxidation rate relationships via the initial assumption that the rate of thickening of the oxide scale is proportional to the flux of the migrating reactant species through the oxide scale, Equation (1). Wagner then assumed that the flux is inversely proportional to the oxide thickness, Equation (2). Integration of Equation (2) yields Equation (3):

Equation for Parabolic Oxide Growth: $$\frac{dL}{dt} = R_c J_c, \quad (1)$$

Fickian Diffusion: $$\frac{dL}{dt} = \frac{k_{parabolic}}{L}, \quad (2)$$

Parabolic Rate Law, ideal case: $$L^2 = 2k_{parabolic}t, \quad (3)$$

Parabolic Rate Law, general case: $$L = (\frac{1}{m}k_{parabolic})^m t^m, \quad (4)$$

where m is the experimentally-determined exponent of the integrated rate law, L is the thickness of the oxide shell, $k_{parabolic}$ is the (parabolic) rate constant, R_c is the oxide volume added per particle of rate limiting species, J_c is the flux or particle current, and t is time. In equation (1), J_c is independent of position within the oxide film (quasi steady state assumption), and the concentrations of the particles (*i.e.*, metal or oxygen ions) are independent of film thickness. The rate constant $k_{parabolic}$ is a function of the temperature, the concentrations of particles at the metal-oxide and oxide-O^- interfaces, the volume of oxide formed, and the diffusion coefficient. While the exponent m has a theoretical value of 0.5, experimental values can vary as a function of the metal type and properties of the oxide shell [6-9].

In the case of high temperature oxidation, the diffusing species may be either metal ions or oxygen ions, and $k_{parabolic}$ is dependent on temperature and the partial pressure of oxygen. The influence of the high temperature environment allows continued oxidation of the metal as ionic species diffuse either outward from the metal-oxide interface to the oxide-oxygen ion (oxide-O^-) interface or inward from the oxide-O^- interface to the metal-oxide interface [10-12]. For

stabilized iron nanoparticles in aqueous environments, other factors may also promote continued oxidation, including the presence of both water and oxygen molecules, the chelating behavior of stabilizers, and defects in the native oxide shell.

B. Low-temperature Oxidation

In contrast, at low (*i.e.*, ambient) temperatures, metal oxidation kinetics are often observed to have logarithmic or inverse logarithmic behavior, with fast initial oxide growth and a sharp decline in oxidation. For logarithmic behavior, the oxidation rate falls to zero as the growth rate nears an asymptote. The kinetics of oxide growth at low temperatures were considered by Cabrera and Mott [11], who described oxide shell formation on a fresh metal surface as a multistage process. Oxidation steps include dissociative adsorption of oxygen at the metal surface, oxidation of the surface metal atoms, ionization of the adsorbed oxygen, incorporation of metal ions into the oxide layer, diffusion of metal ions in the oxide layer, and reactions of metal ions with oxygen ions [5]. The Cabrera-Mott kinetic model describes metal oxidation as two primary consecutive steps: ionic-diffusion-current-controlled oxidation (parabolic behavior) and then electronic-current-controlled oxidation (logarithmic behavior, characterized by electron diffusion, or electron tunneling). Cabrera and Mott described the potential energy difference between the metal-oxide and oxide-O^- interfaces that acts as the driving force for electron migration from one interface to the other; this potential is known as the Mott potential V_M [11, 13]. The Mott potential is the potential energy gradient established by the differences between the work functions of the metal-oxide and oxide-O^- interfaces. The work function is an intrinsic property of any solid face of a particular material and is the minimum energy (eV) required to remove an electron from the material. While the Cabrera-Mott kinetic model works well for

uniform metals and thin films (typically thicknesses less than 10 nm), the theory assumes a perfectly-formed oxide shell with no defects or the presence of bulk charges.

The Cabrera-Mott theory and model was improved by Fromhold and Cook [13], who developed the concept of "coupled currents," which is more applicable to thicker films. With coupled currents theory, the increase in oxide film thickness is a function of both ionic diffusion, or current, and electron tunneling, otherwise known as electronic current. While both currents (*i.e.,* fluxes) occur concurrently during metal oxidation and oxide film formation, the limiting current controls the oxidation rate. Initially, the electric field established across the oxide film is so large that the ionic current controls the oxidation rate. As established by Wagner and further explained by Cabrera and Mott [4, 11], oxidation controlled by ionic diffusion has a parabolic behavior. Thus, the early stage of metal oxidation (*i.e.,* for films of several nanometers thick) should follow Equation (3). As the oxide film thickness increases, the electric field established by the Mott potential decreases, while ionic diffusion remains unaffected by the increase in film thickness. Therefore, the second stage of metal oxidation is controlled by electron tunneling based on a potential difference across the oxide film and follows a logarithmic behavior, Equation (5). Integration of Equation (5) yields Equation (6):

Equation for Logarithmic Oxide Growth: $$\frac{dL}{dt} = \frac{k_{log}}{t+B}, \quad (5)$$

Logarithmic Rate Law: $$L = k_{log} \log(t + B) + A, \quad (6)$$

where k_{log} is the (logarithmic) rate constant, and A and B are temperature-dependent constants. Furthermore, Fromhold and Cook used the assumption that, at steady state, the two currents are equal in magnitude but opposite in sign to calculate the magnitude of the electric field as a function of oxide film thickness [13]. The dependence of the electric field on film thickness is then used with equation (1), where J_c is the rate limiting current. This coupling of flux

equations, set up by their respective diffusing species, accounts for interactions between the two currents and allows the system to reach equilibrium.

C. Iron Oxidation by Oxygen and Water Vapor

More recently, work on iron oxidation in the presence of oxygen gas and water vapor has shown that although the oxidation of iron metal in the presence of oxygen is controlled by ion species diffusion through the oxide film (in agreement with the models presented above), the oxidation of iron metal in the presence of water vapor is controlled at the surface of the oxide [14-16]. Generally, oxidation of a passivated metal surface (and disruption of the passivating oxide) in the presence of water is initiated by anions in solution [17-19]. In the absence of strong anions such as chloride and sulfate, hydroxide anions from water molecules can disrupt the passivating oxide. Grosvenor *et al*. [16] suggested that iron oxidation and the formation of an oxide layer by water vapor is controlled by place exchange, where adsorbed hydroxyl molecules (dissociated from water molecules) exchange positional places with iron atoms at the metal surface. As such, the hydroxyl molecules are incorporated into the metal surface and form the initial metal oxide-hydroxide. Place exchange has also been suggested for the oxidation of other metals [20], and oxidation kinetics controlled by place exchange has been modeled with a direct logarithmic rate law (*e.g*., equation (6)) [16].

D. Nanoparticle Oxidation

Nanoparticles have additional considerations beyond those given for metallic thin films or bulk metals, including the presence of organic stabilizers, and the effect of size and the metal type on oxidation behavior. Metallic nanoparticles are often synthesized in the presence of organic stabilizers that are used to prevent particle aggregation and control particle size. The presence of organic stabilizers will subsequently have an effect on the oxidation rate of the nanoparticles

[21]. In the work of Kanninen *et al*., [21] an increase in the stabilizer concentration caused a delay in copper nanoparticle oxidation. The stabilizer acts as a barrier to the diffusion of oxygen, as well as a binding agent for surface metal ions. Therefore, the presence of organic stabilizer is expected to affect both the initial surface oxidation of a metallic nanoparticle, as well as the bulk oxidation of the metallic core. Auge and coauthors [22] successfully modeled the experimental data of Kanninen *et al*. [21] and predicted an exponential growth rate dependence for the initial stage of a stabilized metallic nanoparticle. This initial exponential growth can be described by the Johnson-Mehl-Avrami-Kolmogorov (JMAK) equation for surface-dominated oxidation at isothermal conditions (room temperature):

$$\frac{dL}{dt} = nk_{JMAK}t^{n-1}exp(-k_{JMAK}t^{n}), \quad \text{and} \tag{7}$$

$$L = -exp(-k_{JMAK}x^{-n}), \tag{8}$$

where n is the Avrami exponent and k_{JMAK} is the (exponential) rate constant [22].

Chernavskii and coauthors calculated the Gibbs free energy change due to the formation of an oxide shell on the surface of a metallic silver nanoparticle as a function of nanoparticle size [5]. Their results showed that, for a specific temperature, below a critical particle diameter, the Gibbs free energy continues to decrease as the thickness of the oxide shell increases. This behavior implies that below a certain size, the oxide shell does not passivate and the particle can completely oxidize. However, for larger particles, the Gibbs free energy first decreases with increasing oxide film thickness and subsequently increases, which implies the formation of a passivating oxide shell. From the work of Chernavskii *et al.* [5], we can expect the nanoparticles synthesized and used in our oxidation study to be large enough to have a passivating oxide shell. However, the oxide shell may not be passivating in an aqueous environment even if the oxide shell is passivating when formed in the presence of oxygen gas due to the incorporation of water

molecules into the shell and subsequent disruption of the shell lattice structure [15, 16]. The QCM results presented in the main article support these previous studies and demonstrate that our iron nanoparticles, which are typically stable in dry air, are quite reactive in an oxygenated aqueous environment, and oxidize within minutes.

III. ADDITIONAL RESULTS & DISCUSSION

A. *TEM*

Transmission electron microscopy (TEM) was used to obtain images of unoxidized ZVI nanoparticles. From these images, a native oxide shell with a thickness of approximately three to five nanometers is observed. Iron metal nanoparticles have been studied with initial anoxic conditions to understand the formation of the native oxide shell that forms upon contact with oxygen. A one-nanometer-thick oxide shell is predicted to form within 0.2 fs and a two-nanometer-thick shell within 40 s [23, 24]. Elemental analysis with TEM confirmed the presence of iron as the primary element, and diffraction patterns indicate the particles are multicrystalline. The internal structure of the ZVI nanoparticles appears to have a unique dendrite-like structure, one that has not been commonly observed in other studies where ZVI nanoparticles have been synthesized by aqueous solution chemistry [25-31]. This dendritic internal structure might result from the interactions of the stabilizers with the growing nanoparticles or from the formation of these particles through irreversible aggregation of smaller particles during synthesis. Differences in crystallinity and internal structure of ZVI nanoparticles might affect the oxidation kinetics, and a comparison of ZVI nanoparticles with different specific morphologies would be necessary to determine how internal morphology influences reactivity.

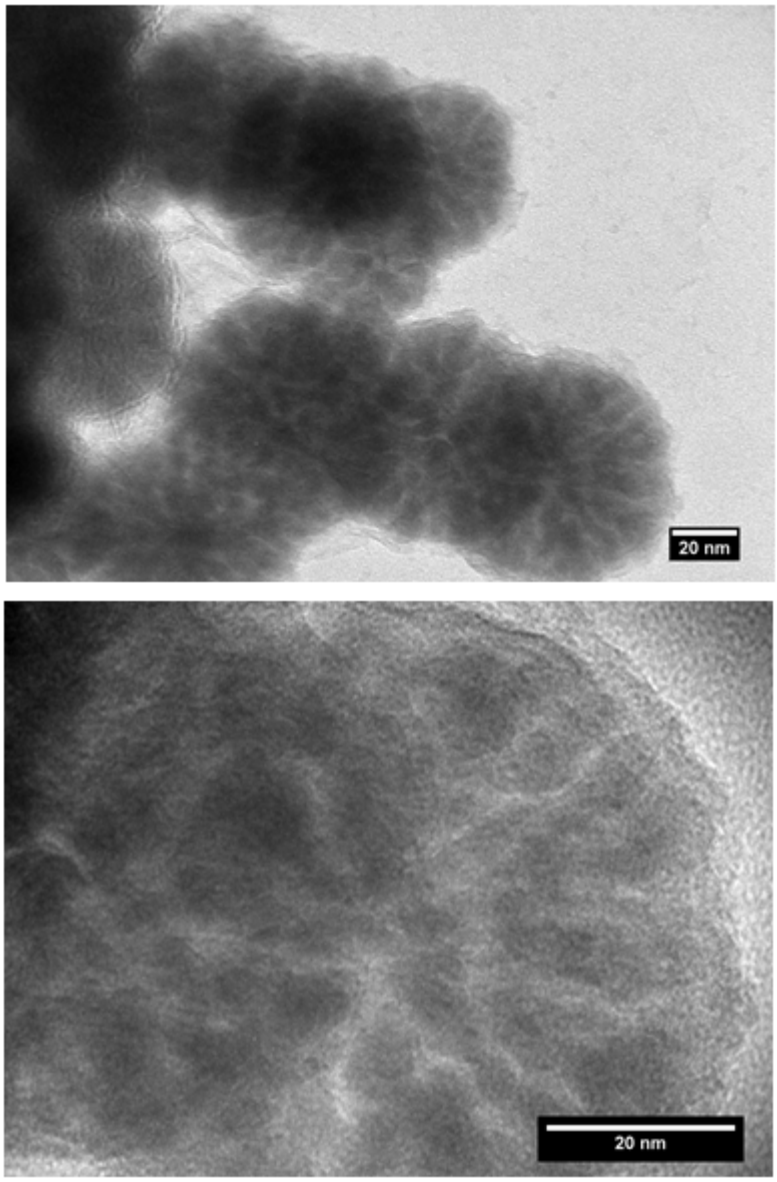

Figure S1. TEM images of unoxidized ZVI nanoparticles. Scale bars are both 20 nm.

TEM images of iron-nickel nanoparticles are shown in Figure S2 for four molar ratios of nickel to iron. As the ratio of nickel to iron increases, the formation of an outer shell on some of the nanoparticles was observed. At higher ratios, a larger number of particles were observed to have this shell, and the internal morphology of the nanoparticles also appears to change. The shell also appears to thicken when the ratio is increased from 100 mmol Ni:mol Fe to 1000 mmol

Ni:mol Fe. At low ratios of nickel to iron, such as at 0.5 mmol Ni:mol Fe, only a few particles were observed to have a shell, or partial shell, formed. At this low ratio, it is possible that the deposited nickel might have formed individual islands in some areas on the surface of the iron particle, but as the nickel to iron ratio increased, it does appear as though the nickel formed a relatively evenly-distributed shell on the nanoparticle surface. As mentioned in the main article, the formation of a shell of nickel was also observed in the work of Lee and Sedlak [32], but in other studies, the deposition of nickel or palladium appeared to form as islands on the iron nanoparticle surface [26, 31, 33]. It is not yet well understood from our work or the work of others why a shell is obtained rather than islands, particularly in the case of iron-nickel nanoparticles where both structures have been reported for similar synthesis techniques [32, 33]. Further studies on these bimetallic nanoparticles will elucidate the crystal phases present and provide information about the core-shell structure of these particles before and after oxidation.

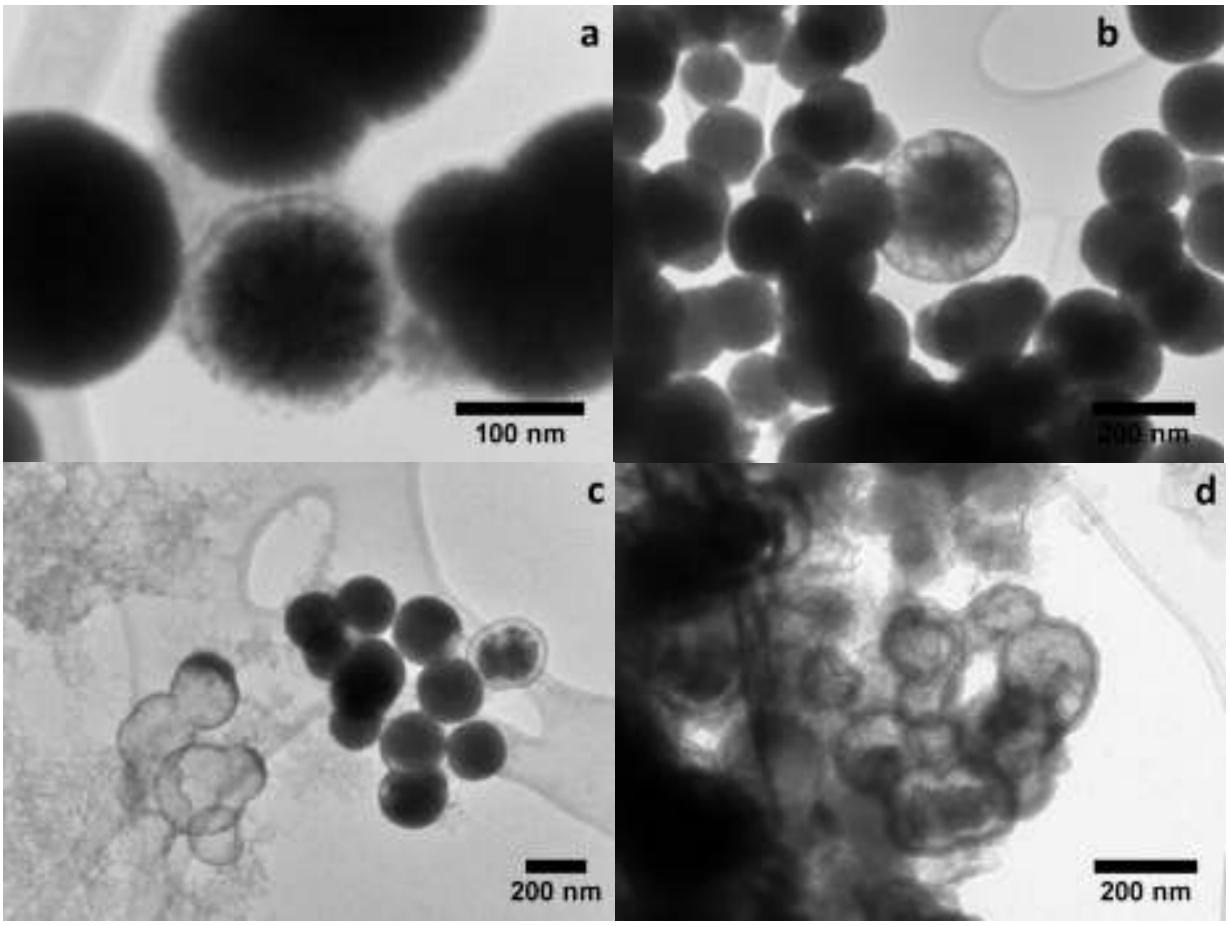

Figure S2. TEM images of iron-nickel nanoparticles for (a) 0.5 mmol Ni:mol Fe, (b) 5 mmol Ni:mol Fe, (c) 100 mmol Ni:mol Fe, and (d) 1000 mmol Ni:mol Fe.

B. XRD

Several unoxidized and oxidized samples were analyzed with XRD (Figure S3). The unoxidized unstabilized sample resulted in narrow peaks in the XRD spectrum, with a primary Fe (110) peak (CuKα, $2\theta = 45^{o}$). Several low intensity peaks for magnetite (Fe_3O_4)/maghemite (γ-Fe_2O_3) were also observed, which is consistent with the presence of a native oxide shell around the iron metal core of the ZVI nanoparticles (TEM images shown in Figure S1). The CMC- and ATMP-stabilized nanoparticle samples resulted in broadened peaks (Figure S3a),

which can indicate the presence of small particles and/or the presence of amorphous metal. Diffraction patterns obtained from TEM indicate that most of the particles are crystalline; however, some particle populations were observed to have no diffraction patterns and might be amorphous. From TEM images, most of the particles observed were approximately 100 nm in diameter, where the iron metal cores of the particles are multi-crystalline. The individual crystallites are approximately 5 nm in diameter and are likely the primary influence in the observed peak broadening.

Based on microscopy and DLS, the particles as synthesized are above the critical size required for iron nanoparticle passivation at ambient temperature [5]. Extensive work at room temperature has shown that the oxide shell formed on single crystal iron is a combination of magnetite and maghemite [34-38]. However, work specifically performed on nanoparticles indicates that the oxide shells may resemble those of bulk iron but will likely have more defects which could affect particle reactivity [39], and the oxide of the passivating shell formed as a result of exposure to oxygen may differ from the oxide formed in the presence of oxygenated water. In this work, when bulk aqueous suspensions of ZVI nanoparticles were shaken, the suspensions either turned orange-red or dark brown. Both samples were shaken for approximately one hour, and the reason for why different oxides were obtained was not investigated further in this study. All bulk samples were taken directly from a CMC-stabilized ZVI nanoparticle synthesis, and the suspensions were bubbled with argon during synthesis. Therefore, it is possible that the different samples had varying dissolved oxygen concentrations, which caused different iron oxides/hydroxides to form. The orange-red sample contained flat plated crystals identical in appearance to the images shown in the main article in Figure 1b and Figure 1d and was determined by XRD (Figure S3b) to be primarily lepidocrocite (γ-FeO(OH)).

In contrast, the dark brown sample contained faceted octahedral particles determined to be primarily magnetite (Fe_3O_4)/maghemite (γ-Fe_2O_3).

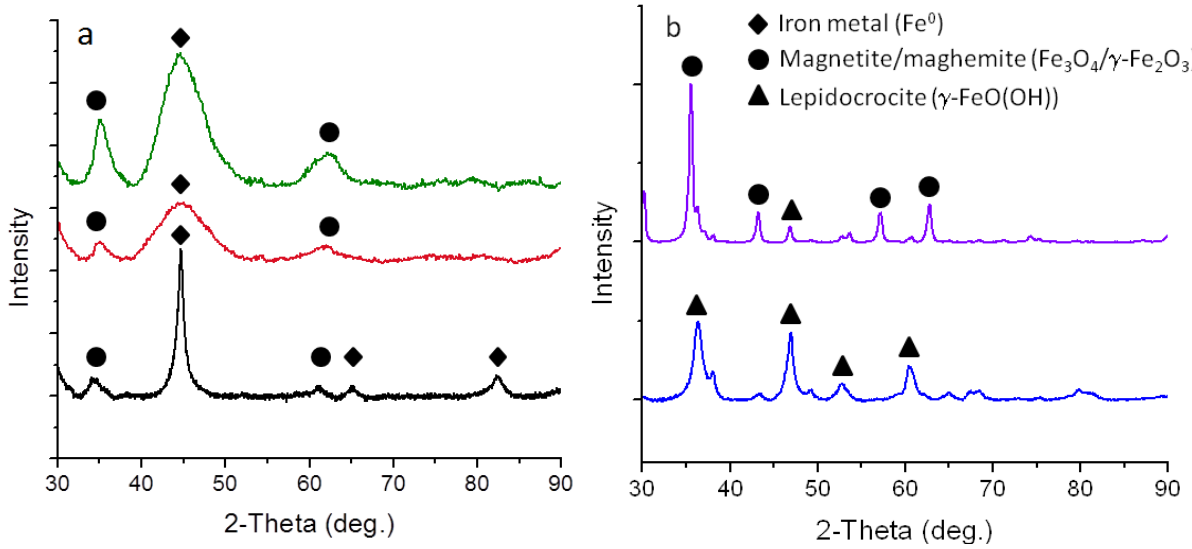

Figure S3. X-Ray Diffraction patterns for ZVI nanoparticles (a) before and (b) after oxidation. The bottom spectrum in part (a) is from an unstabilized ZVI sample. The middle and top spectra of part (a) are of CMC- and ATMP-stabilized ZVI nanoparticle samples, respectively. In part (b), the bottom spectrum (blue curve) is a fully oxidized CMC-stabilized ZVI nanoparticle sample with lepidocrocite as the primary phase, and the top spectrum (purple curve) is a fully oxidized CMC-stabilized ZVI nanoparticle sample composed of approximately 70 % magnetite and 30 % lepidocrocite. Diamonds denote iron metal peaks, circles denote magnetite/maghemite peaks, and triangles denote lepidocrocite peaks.

C. DLS

The oxidation of CMC-stabilized ZVI nanoparticles was characterized by DLS and QCM techniques in real time for several volumetric ratios of ethanol to water (main article, Figure 2,

and Figure S4). Ethanol was chosen as the second solvent because of its known hygroscopic nature. Based on the TEM images, the ZVI nanoparticles were assumed to have a passivated native oxide due to exposure to oxygen, and therefore the results obtained for nanoparticle oxidation would be due to the presence of both water and oxygen in a flowing system. The experimental DLS data for 100 %, 75 %, and 50 % H_2O are shown in Figure S4. Based upon literature [13, 40, 41] and the experimental data, a logarithmic rate law is assumed and applied in solid lines to the 75 % and 50 % H_2O data. The results from DLS measurements indicate that this technique can be used to capture at least a portion of the ZVI nanoparticle oxidation behavior when the kinetics are slowed by the addition of ethanol to the aqueous test solution. However, in comparison to the results obtained by the QCM technique, the DLS technique is limited in its utility; ZVI oxidation in 100 % H_2O occurs too quickly for the instrument to obtain useful data and even at a ratio of 50 % H_2O, only a portion of the logarithmic oxidation behavior is captured. In addition, the initial exponential growth observed in QCM data (main article, Figure 2) is not captured by DLS. Finally, modeling the kinetic oxidation behavior of the nanoparticles through DLS may result in an overestimate of the particle growth due to the periodic stopped flow condition with each DLS measurement [42]. At each point of stopped flow, the system is put into a non-steady-state condition, and the equilibrium between reactant (O_2 and H_2O) transport to the particles and particle oxidation could be disrupted.

Furthermore, SEM images taken (data not shown) of QCM crystals after oxidation by either 75 % H_2O or 50 % H_2O indicated that the oxide formed has the same crystal structure as that of the nanoparticle sample oxidized by 100 % H_2O. Based on this result, the oxide phase is expected to be primarily lepidocrocite for all of the ethanol to water volumetric ratios tested, and the crystal morphology is expected to be elongated, plated crystals. Since the DLS instrument assumes a

spherical particle shape for all measurements, light scattering is perhaps not the optimal choice to follow spherical ZVI nanoparticles as they oxidize to a decidedly non-spherical shape. This problem is demonstrated by the data for 50 % H_2O and 75 % H_2O; DLS measurements (Figure S4) indicate that the increase in ethanol volume increased nanoparticle size and the rate of oxidation, while the QCM data (main article, Figure 3) clearly demonstrate that the increase in ethanol concentration causes a delay in ZVI nanoparticle oxidation and a decrease in the overall mass gain due to oxidation. As a result of these conclusions, only the QCM data were used to model the kinetic behavior of iron nanoparticle oxidation. The DLS data are included here as a comparison to QCM because DLS techniques are often used to characterize nanoparticle size and to demonstrate the challenge of accurately capturing nanoparticle oxidation in real time.

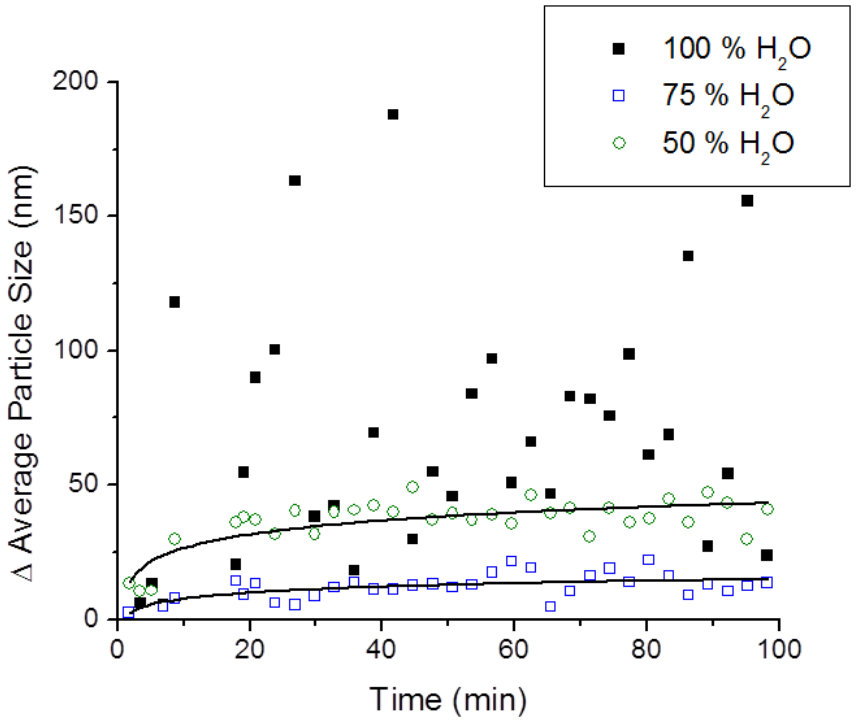

Figure S4. Dynamic light scattering captures a portion of the logarithmic increase in nanoparticle diameter with oxidation. Experimental results are shown as individual data points, while theoretical logarithmic curves (for 75 % H_2O and 50 % H_2O) are shown as solid lines.

DLS experiments were performed at a flow rate of 800 μL/min, where the flow was stopped during each measurement.

D. SEM and EDX of Fe-Ni Nanoparticles

SEM images of unoxidized and oxidized Fe-Ni nanoparticles with a ratio of 5 mmol Ni:mol Fe are shown in Figure S5. The external surface morphology of the unoxidized Fe-Ni nanoparticles generally resembles that of the iron-only nanoparticles, and the oxidized samples contained some elongated structures that resembled the iron oxide hydroxide crystal morphology. The oxidized Fe-Ni nanoparticles generally were observed to have less visible oxide than the iron-only nanoparticles, which supports the QCM data in Figure 3 of the main article; the addition of nickel to the iron nanoparticles, even at low molar ratios such as 5 mmol Ni:mol Fe, appears to prevent the extensive oxidation observed in iron-only nanoparticles.

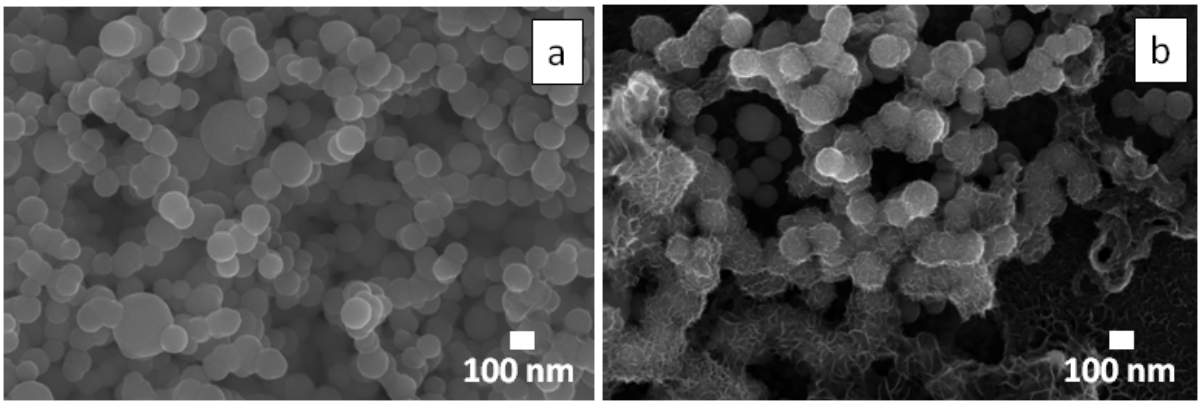

Figure S5. SEM micrographs of ZVI nanoparticles with 5 mmol Ni:mol Fe (a) before and (b) after oxidation.

EDX analysis of unoxidized samples indicated the relative amounts of iron, nickel, and oxygen in the iron-nickel nanoparticles (Table S1). The EDX data indicate that as the amount of nickel

added to the synthesized iron nanoparticles increased, the amount of nickel that reacted and deposited onto the iron nanoparticles also increased, which was expected. However, EDX is only a semi-quantitative technique since no standards are used to compare to samples. It is possible, particularly at higher nickel to iron ratios, that not all of the nickel added to the synthesis solution deposited onto the iron nanoparticles. A fully quantitative technique, such as inductively coupled plasma atomic emission spectroscopy (ICP-AES) would need to be used to determine the precise concentrations of iron and nickel in the different nanoparticle samples. As such, we report in this work the theoretical ratios, whereas the actual amount of nickel in the nanoparticles might be lower.

Table S1. EDX data for unoxidized iron-nickel nanoparticles of different molar ratios of nickel to iron.

Theoretical molar ratio of nickel to iron (mmol Ni:mol Fe)	**Iron (atomic %)**	**Nickel (atomic %)**	**Oxygen (atomic %)**	**Measured Ni:Fe ratio (atomic %:atomic %)**
0.5	50	1	49	0.02
5	48	2	50	0.05
100	46	5	49	0.11
1000	20	8	71	0.42

E. QCM

An original data set from a quartz crystal microbalance (QCM) experiment is presented in Figure S6. This data set shows the change in mass over time for an entire experiment with the following sections: (1) dry, uncoated crystal, (2) dry, nanoparticle-coated crystal, (3) the start of water flow across the crystal, and (4) additional increase in mass that we assume to be primarily caused by the oxidation of the nanoparticles. As mentioned in the main article, QCM measures the resonant frequency of the crystal, and any change to the mass of the sample that is deposited on the crystal will result in a change in the measured resonant frequency. We then use the Sauerbrey equation to then calculate the mass. We have used the QCM data and samples, along with XRD and SEM data, to support our theory that, once exposed to oxygenated water, the iron nanoparticles oxidize primarily to an iron oxide hydroxide, lepidocrocite. However, the change in frequency measured by QCM might also be caused by other mechanisms that are likely occurring in the nanoparticle sample, including dissolution, aggregation, and sorption.

Dissolution of iron ions might occur as the native oxide shell (formed during exposure of the synthesized particles to air) is disrupted by the incorporation of hydroxide ions (i.e., dissociated water molecules), and iron atoms diffuse outward from the iron core to the nanoparticle surface. The dissolution of iron ions is likely to be affected by the stabilizer molecules that are initially on the surface of the nanoparticles; these molecules associate with or chelate with iron cations in solution, and would certainly interact with iron atoms that have diffused to the surface of the particle and dissolved into solution. Stabilizers may act to keep iron atoms near the surface, causing increased oxidation or prevent their oxidation through chelation (primarily in the case of ATMP, a chelator). Stabilizers might also allow iron atoms to migrate to different locations in the sample by providing multiple association sites where the atoms might adsorb and desorb and eventually oxidize or be removed through dissolution into the bulk flowing solution. In the

absence of stabilizers, iron dissolution might result in a loss of mass from the sample, which would lower the overall increase in mass due to oxidation. However, particularly for the CMC-stabilized nanoparticles (Figure 2, main article), we observe an increase in mass consistent with that expected for the oxidation of iron to an iron oxide hydroxide such as lepidocrocite. In the case of ATMP-stabilized iron-only nanoparticles (Figure 3, main article, data represented by a solid black line), we observe that the change in mass is less than that observed in Figure 2 for CMC-stabilized nanoparticles. This reduction in the overall increase in mass might be caused by several mechanisms including iron dissolution and reduced iron oxidation due to chelation.

Particle re-agglomeration and aggregation might also occur during the QCM experiment. The particles are spray coated onto the crystal and are only physically adsorbed to the crystal surface. When the particles are exposed to flowing water, particle movement might occur, with particles becoming redistributed on the surface, particles irreversibly aggregating or combining through Ostwald ripening [43], or particles detaching from the surface to join the bulk liquid flow. Since we can only observe the particles on the crystal surface with SEM before and after the QCM experiments, we do not know, based on our current experimental results, if any of these mechanisms occur with any significance. Future work in the area of liquid cell microscopy would certainly be useful in this research to be able to observe the movement of nanoparticles during an oxidation experiment.

Desorption of molecules, such as the stabilizer compounds or water molecules, would cause a decrease in mass, while adsorption of water molecules would cause an increase in mass. If we carefully observe sections (3) and (4) of the graph in Figure S6, we can see that when water is added to the QCM system, there is an immediate increase in mass. We assume that this first increase in mass is due primarily to the mass of the water added to the crystal, including the

adsorption of water molecules onto the surface of the nanoparticles. After the immediate increase in mass, we then observe a slower increase in mass that generally has the shape of an "S", a shape that has been previously reported and predicted by a model for metal nanoparticle oxidation [5]. While the adsorption and desorption of water molecules might occur throughout the experiment, and stabilizer molecules might also desorb or re-adsorb, changing the overall change in mass measured by QCM, we believe that the QCM data are reflective of nanoparticle oxidation and can still be used, despite the presence of other possible acting mechanisms, to interpret possible mechanisms that occur during oxidation. Particularly with the support of the SEM images and XRD data, as well as a thorough evaluation of the literature to date, we believe the curves we have obtained illustrate oxidation behavior of iron nanoparticles exposed to water. This behavior is observed to be quite similar in shape to oxidation of nanoparticles exposed to oxygen [5] and bulk metals exposed to air or oxygen [11, 13], even though the specific rate constants and onset of oxidation might differ.

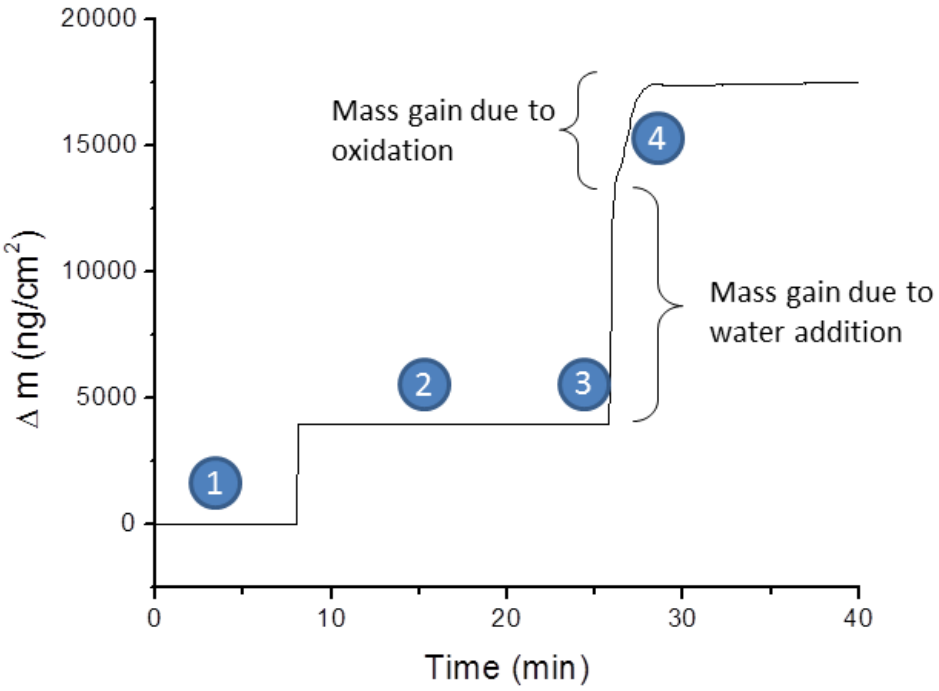

Figure S6. Change in mass as a function of time for a complete QCM experiment.

F. Modeling Results

Modeling results are shown in Figure S7 for the exponential growth regions of the QCM data (normalized change in mass with time). The data were modeled based on Equation 8, by converting the data with the following calculation:

$$x = -\ln\left(-\left(\left(\frac{\Delta m}{m_0}\right) - 1\right)\right), \tag{9}$$

and then graphing x as a function of time. The data were fit with a power law, and the Avrami exponent, n, and the exponential rate constants were obtained.

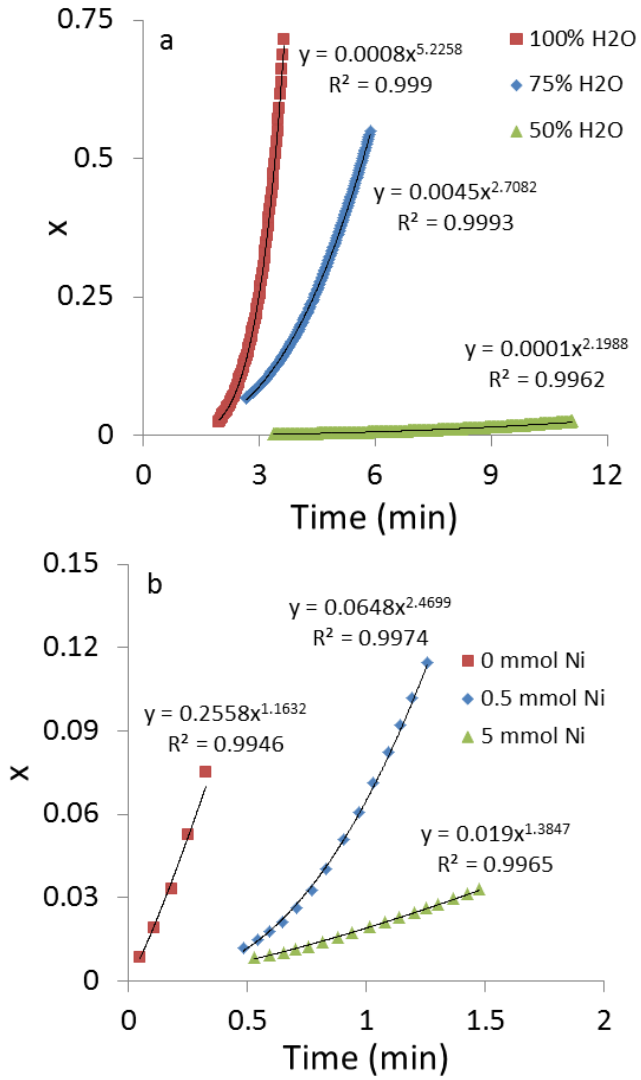

Figure S7. Modeling results for (a) the water-ethanol study and (b) the iron-nickel nanoparticle study. Curve fits are shown for a general power law equation, and the corresponding equations and uncertainties are displayed.

Modeling results are shown in Figure S8 for the logarithmic growth regions (Region 2) of the QCM data based on the rate law described in Equation 6. The logarithmic rate law fits the data well for both the ethanol-water and iron-nickel QCM studies, with the R^2 values ≥ 0.90 in all cases, except for the data set for 100 % H_2O in the ethanol-water study. While it is possible that

other rate laws might also be applied to Region 2 of the data sets, the choice of the logarithmic rate law is consistent with and supported by literature on low temperature oxidation of iron [11, 13], as well as work on metallic nanoparticle oxidation [5, 22]. As a comparison, Region 2 of the QCM data was also modeled using the parabolic rate law of Equation 4; modeling results are shown in Figure S9. The R^2 values range from 0.42 to 0.86, which suggests that the parabolic rate law does not fit the data nearly as well as the logarithmic rate law.

Model	CopyOfLog3P1 Greenlee (User)		
Equation	y = a - b*log(x+c)		
Reduced Chi-Sqr	1.23111E-4		
Adj. R-Square	0.77351		
		Value	Standard Error
100% H2O	a	1.83783	0.001
Z1	b	-0.0222	4.70493E-4
Z1	c	-6.106	0.00741

Model	CopyOfLog3P1Greenlee (User)		
Equation	y = a - b*log(x+c)		
Reduced Chi-Sqr	2.24938E-4		
Adj. R-Square	0.97867		
		Value	Standard Erro
75% H2O	a	1.11988	0.00275
AA1	b	-0.12141	9.45062E-4
AA1	c	-10.9692	0.03001

Model	CopyOfLog3P1		
Equation	y= a - b*log(x+c		
Reduced Chi-Sqr	7.13078E-5		
Adj. R-Square	0.98001		
		Value	Standard Error
AB1	a	0.3794	0.00217
AB1	b	-0.07873	6.82739E-4
AB1	c	-27.4435	0.05138

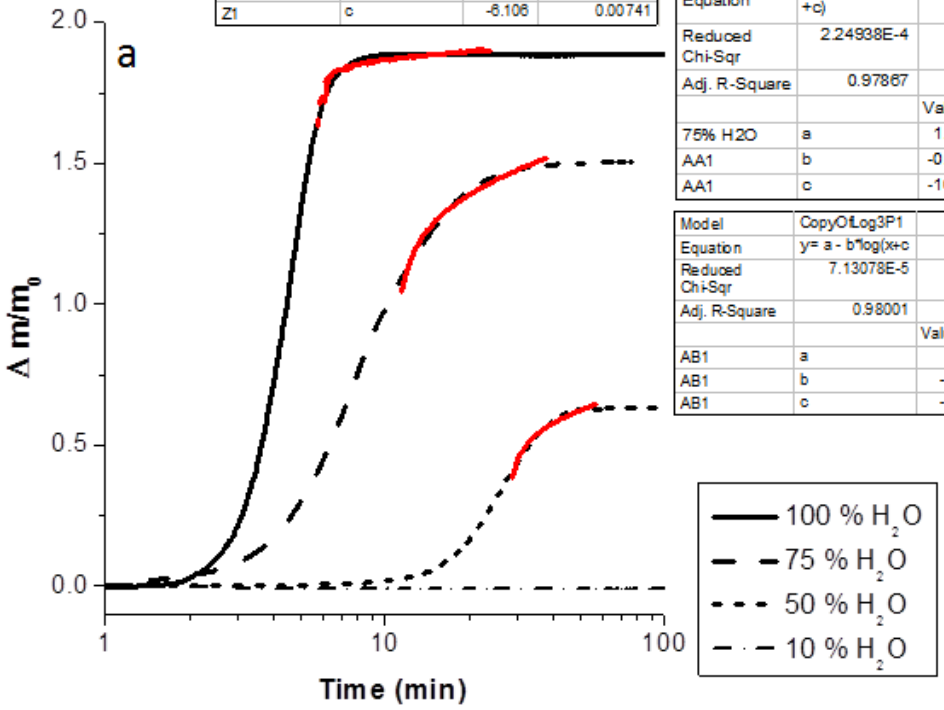

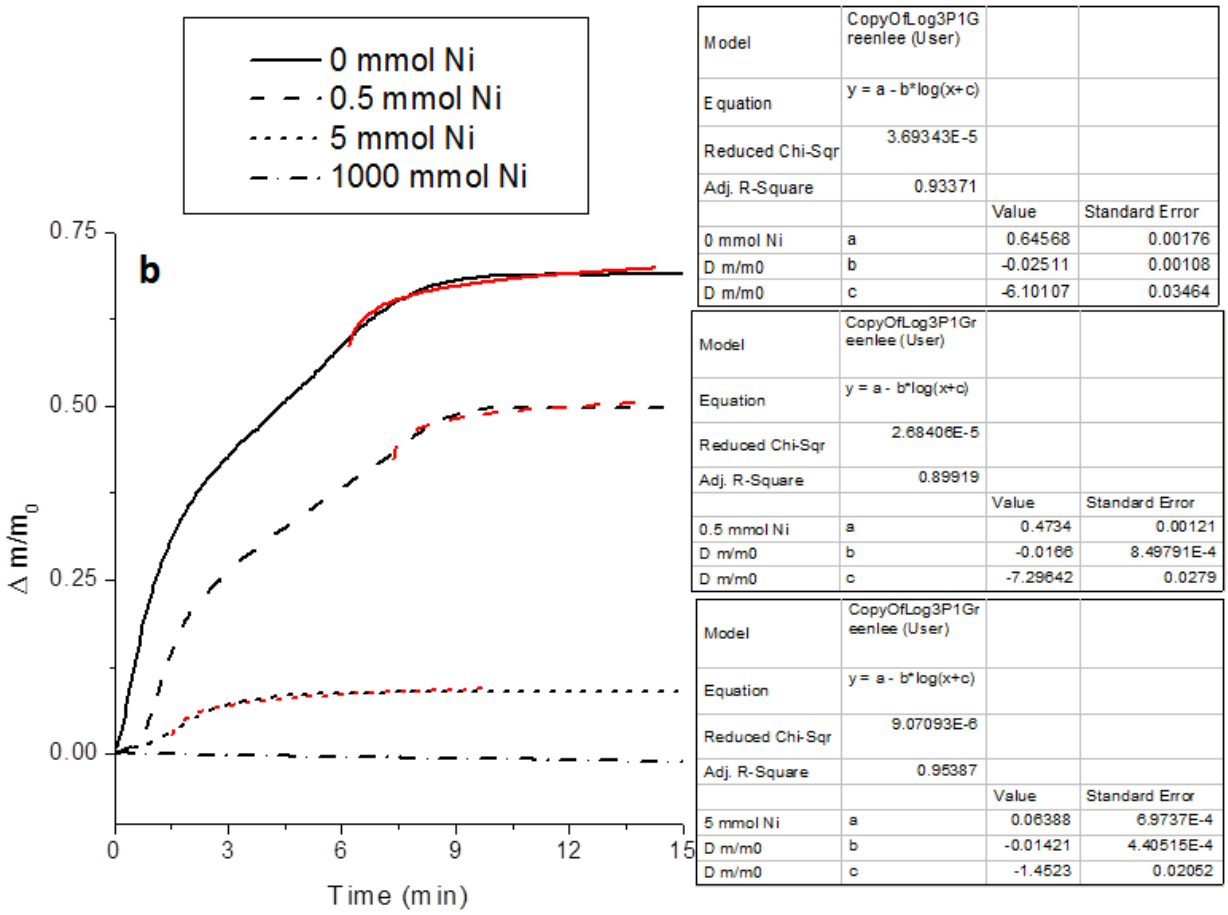

Model	CopyOfLog3P1Greenlee (User)		
Equation	y = a - b*log(x+c)		
Reduced Chi-Sqr	3.69343E-5		
Adj. R-Square	0.93371		
		Value	Standard Error
0 mmol Ni	a	0.64568	0.00176
D m/m0	b	-0.02511	0.00108
D m/m0	c	-6.10107	0.03464

Model	CopyOfLog3P1Greenlee (User)		
Equation	y = a - b*log(x+c)		
Reduced Chi-Sqr	2.68406E-5		
Adj. R-Square	0.89919		
		Value	Standard Error
0.5 mmol Ni	a	0.4734	0.00121
D m/m0	b	-0.0166	8.49791E-4
D m/m0	c	-7.29642	0.0279

Model	CopyOfLog3P1Greenlee (User)		
Equation	y = a - b*log(x+c)		
Reduced Chi-Sqr	9.07093E-6		
Adj. R-Square	0.95387		
		Value	Standard Error
5 mmol Ni	a	0.06388	6.9737E-4
D m/m0	b	-0.01421	4.40515E-4
D m/m0	c	-1.4523	0.02052

Figure S8. Modeling of QCM data using a logarithmic law for (a) the ethanol-water study with iron-only nanoparticles and (b) the iron-nickel nanoparticle study in water.

Model	Allometric1		
Equation	y = a*x^b		
Reduced Chi-Sqr	9.50811E-4		
Adj. R-Squar	0.42067		
100 % H2O		Value	Standard Err
Z1	a	1.7041	0.00735
Z1	b	0.0368	0.00165

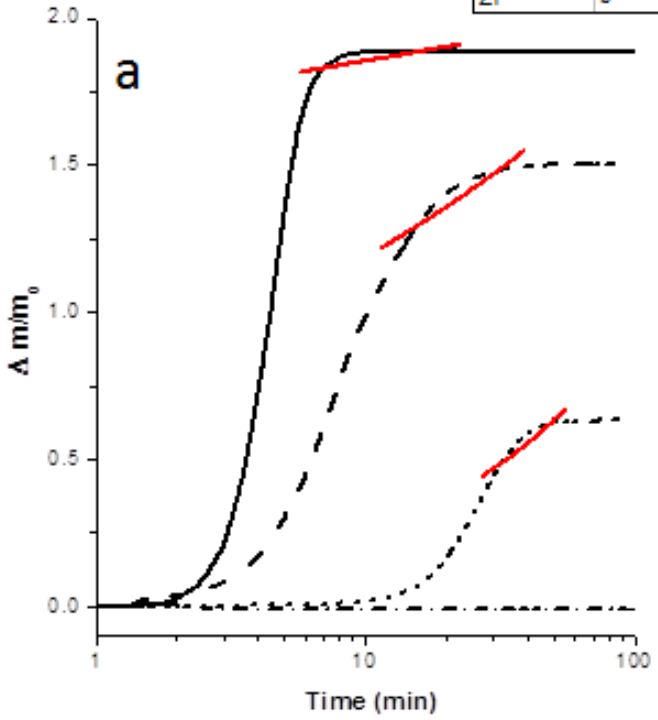

Model	Allometric1		
Equation	y = a*x^b		
Reduced Chi-Sqr	0.00148		
Adj. R-Squar	0.85546		
75 % H2O		Value	Standard Err
AA1	a	0.7564	0.00531
	b	0.1959	0.00218

Model	Allometric1		
Equation	y = a*x^b		
Reduced Chi-Sqr	7.67682E-4		
Adj. R-Square	0.86092		
50 % H2O		Value	Standard Error
AB1	a	0.0652	0.00155
	b	0.58113	0.00634

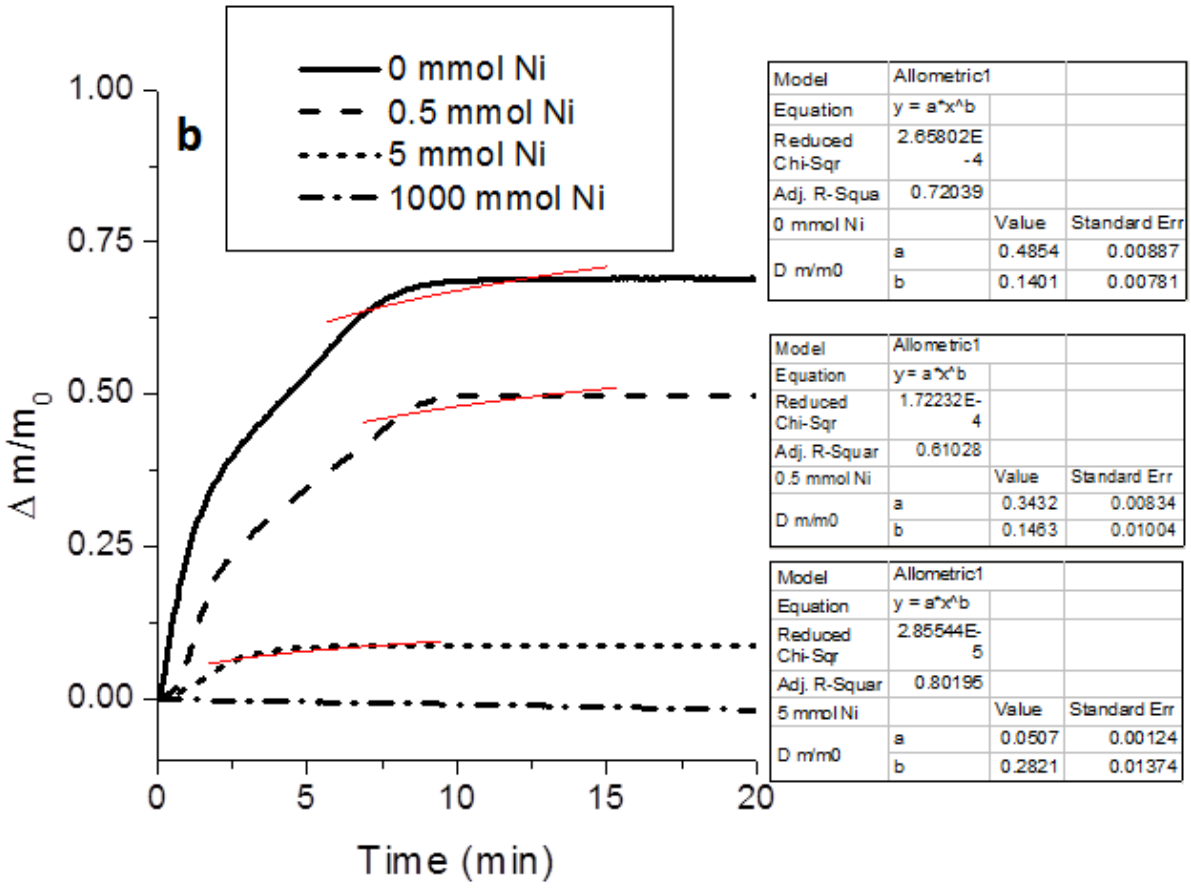

Figure S9. Modeling of QCM data using a parabolic law for (a) the ethanol-water iron-only nanoparticle study and (b) the iron-nickel nanoparticle study.

REFERENCES

1. He, F.; Zhao, D. Y., Manipulating the size and dispersibility of zerovalent iron nanoparticles by use of carboxymethyl cellulose stabilizers. *Environ. Sci. Technol.* **2007,** *41*, (17), 6216-6221.

2. Greenlee, L. F.; Hooker, S. A., Development of stabilized zero valent iron nanoparticles. *Desalin. Water Treat.* **2012,** *37*, 114-121.

3. Sauerbrey, G., Verwendung von Schwingquarzen zur Wägung dünner Schichten und zur Mikrowägung. *Z. Phys.* **1959,** *155*, (2), 206-222.

4. Wagner, C., Reaktionstypen bei der oxydation von legierungen (Reaction types in the oxidation of alloys). *Z. Elektrochem.* **1959,** *63*, (7), 772-790.

5. Chernavskii, P. A.; Peskov, N. V.; Mugtasimov, A. V.; Lunin, V. V., Oxidation of metal nanoparticles: Experiment and model. *Russ. J. Phys. Chem. B* **2007,** *1*, (4), 394-411.

6. Liu, H. W.; Oshida, Y., Grain boundary oxidation and fatigue crack growth at elevated temperatures. *Theor. Appl. Fract. Mec.* **1986,** *6*, (2), 85-94.

7. Reuchet, J.; Remy, L., High temperature fatigue behavior of a cast cobalt-base superalloy. *Fatigue Eng. Mater.* **1979,** *2*, (1), 51-62.

8. Reuchet, J.; Remy, L., Fatigue oxidation interaction in a superalloy-application to life prediction in high temperature low cycle fatigue. *Metall. Trans. A* **1983,** *14*, (1), 141-149.

9. Li, M. H.; Sun, X. F.; Li, J. G.; Zhang, Z. Y.; Jin, T.; Guan, H. R.; Hu, Z. Q., Oxidation behavior of a single-crystal Ni-base superalloy in air. I: At 800 and 900 ^{o}C. *Oxid. Met.* **2003,** *59*, (5-6), 591-605.

10. Fromhold, A. T.; Cook, E. L., Kinetics of oxide film growth on metal crystals: Thermal electron emission and ionic diffusion. *Phys. Rev.* **1967,** *163*, (3), 650-664.

11. Cabrera, N.; Mott, N. F., Theory of the oxidation of metals. *Rep. Prog. Phys.* **1949,** *12*, 163-184.

12. Khanna, A. S., *Introduction to high temperature oxidation and corrosion*. ASM International: Materials Park, OH, 2002.

13. Fromhold, A. T.; Cook, E. L., Kinetics of oxide film growth on metal crystals: Electron tunneling and ionic diffusion. *Phys. Rev.* **1967,** *158*, (3), 600-612.

14. Roosendaal, S. J.; Bakker, J. P. R.; Vredenberg, A. M.; Habraken, F. H. P. M., Passivation of iron oxidation in H_2O and O_2/H_2O mixtures. *Surf. Sci.* **2001,** *494*, (3), 197-205.

15. Grosvenor, A. P.; Kobe, B. A.; McIntyre, N. S., Studies of the oxidation of iron by air after being exposed to water vapour using angle-resolved X-ray photoelectron spectroscopy and QUASES. *Surf. Interface Anal.* **2004,** *36*, (13), 1637-1641.

16. Grosvenor, A. P.; Kobe, B. A.; McIntyre, N. S., Activation energies for the oxidation of iron by oxygen gas and water vapour. *Surf. Sci.* **2005,** *574*, (2-3), 317-321.

17. Isaacs, H. S., Localized breakdown and repair of passive surfaces during pitting. *Corros. Sci.* **1989,** *29*, (2/3), 313-323.

18. Louchel, B. P.; Strehblow, H.-H., On the mechanism of breakdown of passivity of iron for instationary conditions. *Werkst. Korros.* **1980,** *31*, 353-358.

19. Strehblow, H.-H., Breakdown of pssivity and localized corrosion: Theoretical concepts and fundamental experimental results. *Werkst. Korros.* **1984,** *35*, 437-448.

20. Nagy, Z.; You, H., Applications of surface X-ray scattering to electrochemistry problems. *Electrochim. Acta* **2002,** *47*, (19), 3037-3055.

21. Kanninen, P.; Johans, C.; Merta, J.; Kontturi, K., Influence of ligand structure on the stability and oxidation of copper nanoparticles. *J. Colloid Interf. Sci.* **2008,** *318*, (1), 88-95.

22. Auge, A.; Weddemann, A.; Vogel, B.; Wittbracht, F.; Hutten, A., A level set based approach for modeling oxidation processes of ligand stabilized metallic nanoparticles. *Appl. Phys. Lett.* **2010,** *96*, (9), 09311(3).

23. Linderoth, S.; Morup, S.; Bentzon, M. D., Oxidation of nanometer-sized iron particles. *J. Mater. Sci.* **1995,** *30*, 3142-3148.

24. Fung, K. K.; Qin, B.; Zhang, X. X., Passivation of [alpha]-Fe nanoparticle by epitaxial [gamma]-Fe2O3 shell. **2000,** *286*, (1), 135-138.

25. Kim, J. H.; Tratnyek, P. G.; Chang, Y. S., Rapid dechlorination of polychlorinated dibenzo-p-dioxins by bimetallic and nanosized zerovalent iron. *Environ. Sci. Technol.* **2008,** *42*, (11), 4106-4112.

26. Chun, C. L.; Baer, D. R.; Matson, D. W.; Amonette, J. E.; Penn, R. L., Characterization and reactivity of iron nanoparticles prepared with added Cu, Pd, and Ni. *Environ. Sci. Technol.* **2010,** *44*, (13), 5079-5085.

27. Hwang, Y. H.; Kim, D. G.; Shin, H. S., Effects of synthesis conditions on the characteristics and reactivity of nano scale zero valent iron. *Appl. Catal. B-Environ.* **2011,** *105*, (1-2), 144-150.

28. Kim, H.-S.; Ahn, J.-Y.; Hwang, K.-Y.; Kim, I.-K.; Hwang, I., Atmospherically stable nanoscale zero-valent iron particles formed under controlled air contact: Characteristics and reactivity. *Environ. Sci. Technol.* **2010,** *44*, (5), 1760-1766.

29. Li, X.-q.; Elliott, D. W.; Zhang, W.-x., Zero-valent iron nanoparitcles for abatement of environmental pollutants: Materials and engineering aspects. *Crit. Rev. Solid State* **2006,** *31*, 111-122.

30. Nurmi, J. T.; Tratnyek, P. G.; Sarathy, V.; Baer, D. R.; Amonette, J. E.; Pecher, K.; Wang, C. M.; Linehan, J. C.; Matson, D. W.; Penn, R. L.; Driessen, M. D., Characterization and properties of metallic iron nanoparticles: Spectroscopy, electrochemistry, and kinetics. *Environ. Sci. Technol.* **2005,** *39*, (5), 1221-1230.

31. Zhu, B.-W.; Lim, T.-T., Catalytic reduction of chlorobenzenes with Pd/Fe nanoparticles: Reactive sites, catalyst stability, particle aging, and regeneration. *Environ. Sci. Technol.* **2007,** *41*, 7523-7529.

32. Lee, C.; Sedlak, D. L., Enhanced formation of oxidants from bimetallic nickel-iron nanoparticles in the presence of oxygen. *Environ. Sci. Technol.* **2008,** *42*, (22), 8528-8533.

33. Schrick, B.; Blough, J. L.; Jones, A. D.; Mallouk, T. E., Hydrodechlorination of trichloroethylene to hydrocarbons using bimetallic nickel-iron nanoparticles. *Chem. Mater.* **2002,** *14*, (12), 5140-5147.

34. Leibbrandt, G. W.; Hoogers, G.; Habraken, F. H. P. M., Thin oxide film growth on Fe (100). *Phys. Rev. Lett.* **1992,** *68*, (12), 1947-1950.

35. Brundle, C. R.; Chuang, T. J.; Wandelt, K., Core and valence level photoemission studies of iron oxide surfaces and the oxidation of iron. *Surf. Sci.* **1977,** *68*, 459-468.

36. Roosendaal, S. J.; Asseelen, B. v.; Elsenaar, J. W.; Vredenberg, A. M.; Habraken, F. H. P. M., The oxidation state of Fe (100) after initial oxidation in O_2. *Surf. Sci.* **1999,** *442*, (3), 329-337.

37. Simmons, G.; Dwyer, D. J., A LEED-AES study of the initial stages of oxidation of Fe (001). *Surf. Sci.* **1975,** *48*, (2), 373-392.

38. Ruckman, M. W.; Chen, J.; Strongin, M., Oxidation of iron films at 25 K and the reactive oxidation of iron in solid oxygen. *Phys. Rev. B* **1992,** *45*, (24), 14273-14278.

39. Wang, C. M.; Baer, D. R.; Amonette, J. E.; Engelhard, M. H.; Antony, J.; Qiang, Y., Morphology and electronic structure of the oxide shell on the surface of iron nanoparticles. *J. Am. Chem. Soc.* **2009,** *131*, (25), 8824-8832.

40. Martin, M.; Fromm, E., Low-temperature oxidation of metal surfaces. *J. Alloy Compd.* **1997,** *258*, (1-2), 7-16.

41. Rhodin, T. N., Low temperature oxidation of copper. I. Physical mechanism. *J. Am. Chem. Soc.* **1950,** *72*, (11), 5102-5106.

42. Birks, N.; Meier, G. H.; Pettit, F. S., *Introduction to high temperature oxidation of metals*. 2nd ed.; Cambridge University Press: Cambridge, UK, 2006.

43. Boistelle, R.; Astier, J. P., Crystallization Mechanisms in Solution. *J. Cryst. Growth* **1988,** *90*, (1-3), 14-30.